Journal of Energy Storage 144 (2026) 119828

Contents lists available at ScienceDirect

Journal of Energy Storage

journal homepage: www.elsevier.com/locate/est

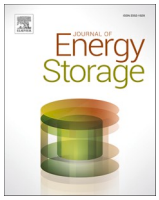

Research papers

Synergistic effects of ionic liquid and redox species for improved aqueous-based Zn-ion capacitor

Emine Kapancik Ulker [a,b], Kazem Mohammadzadeh [a], Abhishek Lahiri [a,*]

[a] Department of Chemical Engineering, College of Engineering, Design and Physical Science, Brunel University of London, Kingston Lane, Uxbridge, Middlesex, UB8 3PH, United Kingdom
[b] Department of Chemistry, Faculty of Arts and Science, Recep Tayyip Erdogan University, Rize, 53100, Turkey

ARTICLE INFO

Keywords:
Zinc ion capacitor
Redox-active electrolyte
Ionic liquids
Graphene
1-Ethyl-3-methylimidazolium iodide

ABSTRACT

As the demand for high-performance energy storage devices grow, aqueous zinc-ion hybrid capacitors (ZICs) have gained significant attention for their ability to combine the high energy density of zinc-ion batteries (ZIBs) with the high-power density of supercapacitors (SCs). However, their application is limited by poor stability caused by zinc dendrite growth from uneven Zn deposition/stripping. Ionic liquids (ILs) and redox species in ZICs are an emerging area of research focused on improving the performance and efficiency of energy storage devices. The combination of IL and redox species can enhance the charge storage capacity, stability, and cycling performance of ZICs, potentially providing high energy and power densities with long-term durability. Herein, synergistic effects of 1-Ethyl-3-methylimidazoliumtriflate (EMImTfO) and 1-Ethyl-3-methylimidazolium iodide (EMImI) were investigated on aqueous electrolyte of $Zn(TfO)_2$. The Zn/graphene ZIC delivers capacities of 82 and 96 mAh g^{-1} at 0.5 A g^{-1} in $Zn(TfO)_2$ and $Zn(TfO)_2$/ EMImTfO electrolytes, respectively, while the redox additive of EMImI boosts the capacity to 182 mAh g^{-1} under the same conditions. Moreover, even at a high current density of 5 A g^{-1}, the capacity was found to be 100 mAh g^{-1}, indicating improved rate capability. These findings offer a promising strategy for the development of redox-active electrolytes tailored for next-generation sustainable energy storage systems.

1. Introduction

Given the growing prevalence and adoption of smart grids and electric vehicles, the demand for energy storage devices, such as rechargeable metal-ion batteries and electrochemical capacitors is rising [1,2]. Among various storage systems, aqueous zinc-ion hybrid capacitors (ZICs) have garnered considerable attention due to their ability to integrate the high energy density of zinc-ion batteries (ZIBs) with the superior power density of supercapacitors (SCs) [3]. Besides, Zn metal offers several advantages, including a high volumetric capacity (5845 mAh cm^{-3}), a low redox potential (−0.76 V vs SHE), cost-effectiveness, non-toxicity and abundant availability. However, its application is hindered by poor stability caused by zinc dendrite growth from uneven Zn deposition/stripping, water decomposition and by-product formations. These reactions lead to a decrease in Coulombic efficiency (CE), thereby resulting in energy loss in ZICs [2,4].

The electrolyte choice is an important factor of ZICs, as it not only facilitates the migration of Zn ions but also affects the capacitor's performance and cycle life [5,6]. Aqueous electrolytes have been studied largely in ZICs. However, they face several challenges, including limited electrochemical window (EW), the formation of Zn dendrites, hydrogen evolution reaction (HER), and the generation of non-conductive passivation by-products in the electrolyte [7]. The solvation structure of Zn in the electrolyte can be regulated by the use of additives to overcome the above challenges for improved performance [8]. In comparison to aqueous electrolytes, ionic liquids have gained significant attention in ZICs due to their unique properties, such as high ionic conductivity, wide electrochemical windows, and low volatility [9]. The use of ILs in ZICs can enhance performance by improving energy density and cycling stability, as they can operate over a broader potential range compared to conventional aqueous electrolytes. Additionally, ILs offer better safety characteristics by reducing risks like leakage and evaporation, making them ideal for high-performance applications. Their tuneable properties also allows to address specific challenges in ZICs, such as mitigating dendrite growth and improving charge-discharge efficiency [10,11]. A promising approach to enhance

* Corresponding author.
E-mail address: abhishek.lahiri@brunel.ac.uk (A. Lahiri).

https://doi.org/10.1016/j.est.2025.119828
Received 22 September 2025; Received in revised form 11 November 2025; Accepted 7 December 2025
Available online 15 December 2025

the specific capacitance of supercapacitors involves the use of redox-active species such as metal ions, halide anions, and active molecules to promote redox reactions on the electrode surfaces, thereby significantly increasing both capacitance and energy density. The implementation of redox couples can be achieved in two ways: i) redox species can be added to the electrolyte, where they participate in faradaic reactions during the charge and discharge processes [12–20], and ii) redox-active species can be incorporated into the cathode material, modifying its electrochemical properties to enhance the device's overall performance [21,22]. Both approaches aim to improve capacitance and energy density by introducing additional redox reactions into the electrochemical process. It has recently been shown that the redox additives, including anthraquinone-based molecules [12], ($3Br^-/Br_3^-$) [13], and methyl viologen (MV)/bromide [14], enhanced the capacity and energy density of ZICs. Mixed electrolyte of 1-ethyl-3-methylimidazolium halide (EMImX) with the ILs of 1-ethyl-3-methylimidazolium tetrafluoroborate ($EMImBF_4$) [23,24] and 1-ethyl-3-methylimidazolium bis (trifluoromethyl sulfonyl) imide ([Emim][TFSI]) [25] provided pseudocapacitance by Faradaic reactions, increasing capacity.

Among the various cathode materials, carbon-based materials have been extensively researched [26–28]. However, the overall electrochemical performance of most carbon-based cathodes reported to date remains well below the practical requirements [29]. Therefore, to enhance the overall electrochemical performance of ZICs, a cathode material with a high specific surface area (SSA) and suitable porosity is essential to facilitate efficient Zn^{2+} ion adsorption/desorption, along with exhibiting high surface redox activity. Since its initial discovery, graphene has garnered significant attention due to its superior properties such as excellent electronic conductivity, large SSA, large intrinsic electron mobility, and high porosity [30]. Due to these distinct properties, graphene and its derivatives stand out as highly promising cathode materials for ZICs [31–35].

In this study we show the enhancement in the performance of ZICs by adding both ionic liquid electrolytes and redox species in Zn salt containing aqueous solution. Herein, synergistic effects of EMImTfO and EMImI were investigated on aqueous electrolyte of $Zn(TfO)_2$. In the hybrid electrolyte, graphene delivered a capacity of 100 mAh g^{-1} at a current density of 5 A g^{-1}, representing a twofold enhancement compared to its performance in the aqueous electrolyte.

2. Experimental methods

2.1. Chemicals

Graphene was purchased from Nanografi (99.9 %), Carbon black was supplied from C-NERGY. Polyvinylidene fluoride (PVDF) and 1-methyl-2-pyrrolidinone (NMP) (99.5 %) were obtained from Sigma-Aldrich. The ionic liquid, EMImTfO was purchased from IOLI-TEC, Germany (99 %) and EMImI was purchased from Alfa Aesar (97 %). $Zn(TfO)_2$ were obtained from Thermo Scientific (98 %). Scheme 1 shows the molecular structures of EMImTfO and EMImI. The solutions were prepared with different concentrations of EMImTfO and EMImI in 2 M $Zn(TfO)_2$.

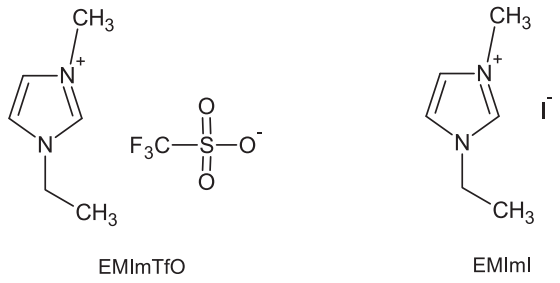

Scheme 1. Molecular structures of EMImTfO and EMImI

2.2. Preparation of graphene

Graphene solution was prepared by mixing graphene, PVDF and carbon black in a weight ratio of 9:0.5:0.5 to obtain a total mass of 4 g. Initially, 0.2 g of PVDF was dissolved in NMP under continuous stirring for approximately 24 h until a clear solution was obtained. Subsequently, 3.6 g of graphene and 0.2 g of carbon black were added to the solution, and the resulting mixture was homogenised at 4000 rpm for 1 h using a high-speed homogeniser to ensure uniform dispersion. The graphene cathode was prepared by drop-casting 50 μL of graphene dispersion on carbon paper (CP), followed by drying at 70 °C overnight. The mass loading of graphene was 1.6 mg cm^{-2}.

2.3. Instruments

Shimadzu IR spirit was used to acquire FTIR spectra. A drop of the electrolyte was put onto the ATR and IR spectra was measured from 4000 to 600 cm^{-1} at a resolution of 4 cm^{-1}.

Raman spectra of graphene electrode were acquired using Renishaw inVia confocal Raman microscope, equipped with a 514 nm laser (Stellar-REN) and using a diffraction grating of 1800 lines/mm with a Renishaw CCD camera as the detector, respectively. For Raman, the samples were run with laser power at 100 % using the 5× objective lens with a 532 nm laser, respectively.

XPS Analysis was performed using a Thermo NEXSA XPS fitted with a monochromated Al kα X-ray source (1486.7 eV), a spherical sector analyser and 3 multichannel resistive plate, 128 channel delay line detectors. All data was recorded at 19.2 W and an X-ray beam size of 400 × 200 μm. Survey scans were recorded at a pass energy of 200 eV, and high-resolution scans recorded at a pass energy of 40 eV. Electronic charge neutralization was achieved using a Dual-beam low-energy electron/ion source (Thermo Scientific FG-03). Ion gun current = 150 μA. Ion gun voltage = 45 V. All sample data were recorded at a pressure below 10–8 Torr and a room temperature of 294 K. Data were analysed using CasaXPS v2.3.20PR1.0.

2.4. Electrochemical measurements

Electrochemical measurements were performed in a bespoke cell containing graphene-coated CP as a cathode, 2 M $Zn(TfO)_2$ with and without ionic liquids as an electrolyte, and a Zn plate as an anode, respectively. Before the experiments, the Zn plates were mechanically polished to remove the oxide layer. Cyclic voltammetry (CV) and galvanostatic charge−discharge (GCD) experiments were carried out using a Biologic potentiostat/galvanostat VMP 3E controlled by EC-Lab software. Long-term cycling experiments were performed using a battery tester (NanoCycler).

The corrosion and hydrogen evolution behaviour of Zn anode in three different electrolytes was studied using an electrochemical cell with a Zn plate as the working electrode, a carbon plate as the counter electrode, and Ag/AgCl as the reference electrode. The Tafel corrosion measurements were conducted within a potential range of −0.7 V to −1.2 V (vs. Ag/AgCl) at a scan rate of 5 mV s^{-1}. The performance of the HER was evaluated by Linear Sweep Voltammetry (LSV) in the potential range of −0.9 V to −1.1 V vs. Ag/AgCl at a scan rate of 5 mV s^{-1}.

3. Results and discussion

3.1. Characterisation of the electrolytes

To investigate the structural changes induced by the addition of EMImTfO and EMImI to the $Zn(TfO)_2$ electrolyte, FTIR and Raman spectroscopic analyses were carried out. Fig. 1a compares the FTIR of 2 M $Zn(TfO)_2$ in the presence and absence of EmimTfO and EmimI. The FTIR spectrum of $Zn(TfO)_2$ exhibits prominent peaks at 1029 cm^{-1} and 1245 cm^{-1}, attributed to the symmetric and asymmetric stretching

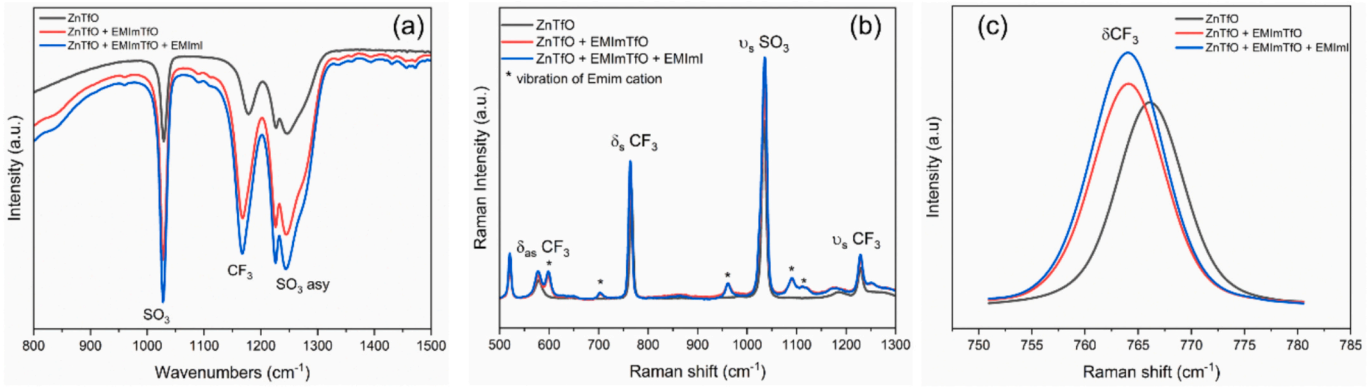

Fig. 1. (a) Comparison of FTIR of aqueous and aqueous-ionic liquid electrolytes (b) Raman spectra showing the changes in the vibrations in aqueous and aqueous-ionic liquid electrolyte (c) The changes in the Raman spectra between 750 and 785 cm^{-1}.

vibration of the SO_3 group, at 1178 cm^{-1} and 1226 cm^{-1}, attributed to the asymmetric and symmetric stretching vibration of CF_3 (Fig. 1a) [36,37]. With the addition of ionic liquid, shifts in the CF_3 and SO_3 stretching are observed, which can be related to the change in the Zn solvation structure. Similar spectral features and trends were also observed in the Raman spectra, supporting the FTIR results and further confirming the structural modification induced by the addition of ionic liquids. The Raman spectra of the electrolytes between 500 and 1300

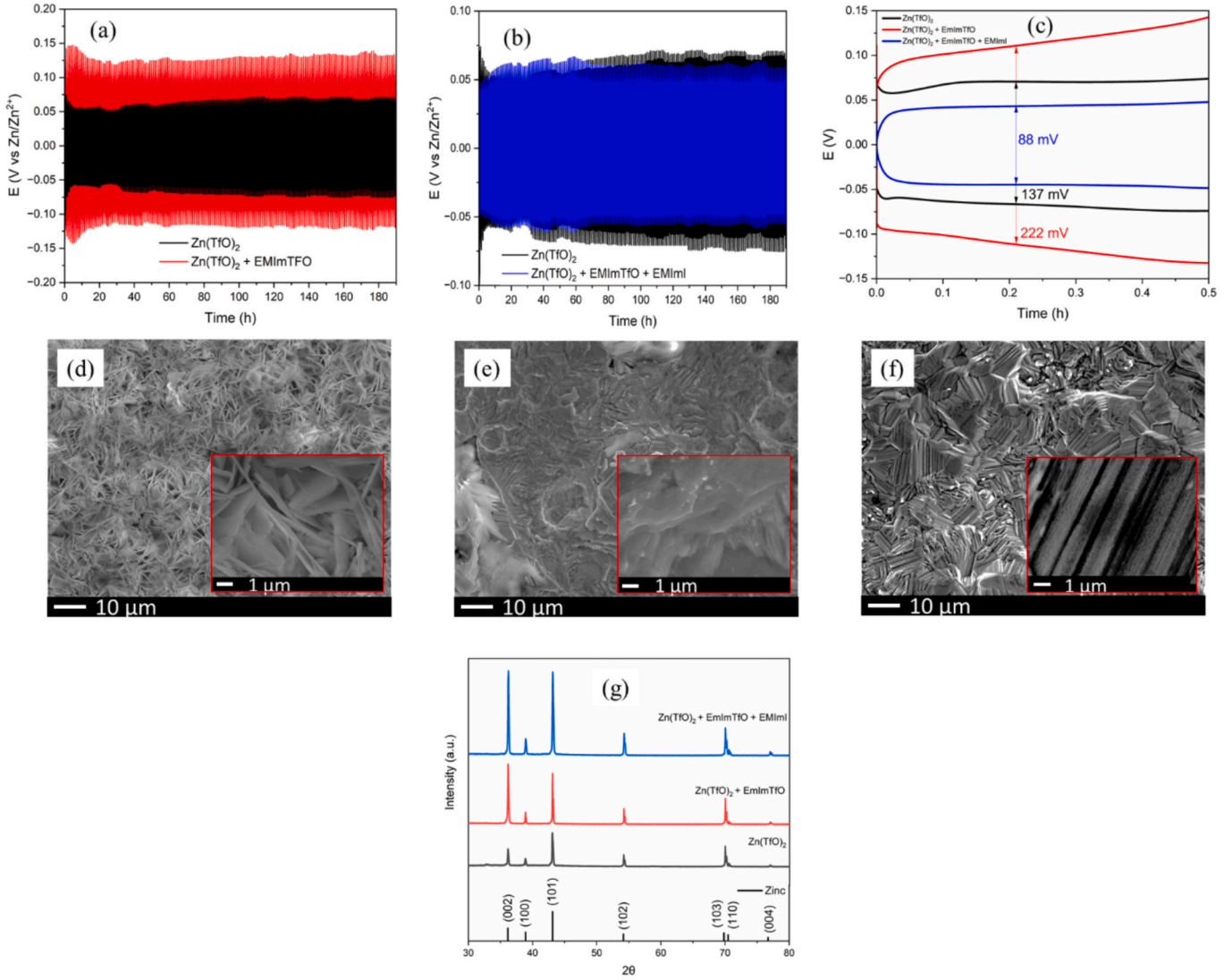

Fig. 2. a,b) Comparison of Zn plating/stripping in a Zn/Zn symmetric cell with all electrolytes at 2 mA cm^2 with a sweep duration of 30 min over 190 h, c) charge and discharge over-voltage of all electrolytes, SEM of Zn anode after 190 charge/discharge cycles from (d) 2 M $Zn(TfO)_2$, (e) 2 M $Zn(TfO)_2$ + 1.33 M EMImTfO, (f) 2 M $Zn(TfO)_2$ + 1.33 M EmimTfO +50 mM EMImI and g) XRD of Zn anode after long-term galvanostatic test with three electrolytes.

cm^{-1} are compared in Fig. 1b. The symmetric stretching $\nu_s(CF_3)$, the symmetric stretching $\nu_s(SO_3)$, the symmetric deformation $\delta_s(CF_3)$, and the asymmetric deformation $\delta_{as}(CF_3)$ modes are observed at 1229, 1034, 766, and 577 cm^{-1}, respectively [38]. The symmetric deformation $\delta_s(CF_3)$ red shifted to 764 cm^{-1} with the addition of ionic liquid (Fig. 1c). This can be attributed to the displacement of water molecules, which initially formed strong hydrogen bonds with the triflate anions. The replacement of water by ionic liquids reduces hydrogen bonding strength in the local environment, correspondingly decreases the vibrational energy. This result is consistent with previous literature [38].

Next, we investigated the impact of three electrolytes on the Zn anode using Tafel plot and LSV measurement. In the Tafel analysis, corrosion potential remained nearly identical in all the electrolytes, suggesting that the additive does not significantly alter the Zn corrosion potential. The results are shown in Fig. S1a, and the corrosion potentials are summarized in Table S1. In addition, HER property of the Zn anode in these electrolytes was performed by LSV in a potential range of −0.9 V to −1.1 V. As shown in Fig. S1b, the addition of IL to aqueous $Zn(TfO)_2$ electrolyte increased the hydrogen overpotential, indicating that it helps suppress side reactions, in agreement with previous study [39]. In comparison, the electrolyte of $Zn(TfO)_2$ + EMImTfO + EMImI exhibits a higher overpotential at the current density of 10 mA cm^{-2} compared to the aqueous electrolyte, suggesting a reduction in hydrogen evolution during Zn deposition/stripping [40].

3.2. Cycling stability

To assess the feasibility of the electrolyte ($Zn(TfO)_2$ + EMImTfO + EMImI) toward the practical application, Zn deposition/stripping behaviour was investigated in a Zn/Zn symmetric cell at a current density of 2 mA cm^{-2}. The voltage profiles are compared in Fig. 2a,b. Zn deposition/stripping process remained stable for over 190 h in all electrolytes. In $Zn(TfO)_2$ aqueous electrolyte, the charge and discharge over-voltage increased after 30 h and then, stabilised at 137 mV. However, the addition of EMImTfO led to an increase in over-voltage up to 222 mV, which can be attributed to the change in the Zn speciation as observed from the Raman studies. With the addition of the redox electrolyte, the over-voltage decreased to 88 mV (Fig. 2c). This improvement may be due to the enhanced charge transfer kinetics facilitated by the redox-active species, which promotes more efficient Zn deposition/stripping processes. The Zn anode was analysed after 190 charge/discharge cycles to evaluate the possibility of dendritic growth. Zn electrode demonstrated excellent long-term cycling performance with all electrolytes, suggesting dendrite-free morphology (Fig. 2d-f). Fig. 2g presents the XRD patterns of Zn electrodes after long-term galvanostatic cycling, providing insight into the influence of electrolyte composition on deposition behaviour. All diffraction profiles matched standard Zn (ICDD 78–9363), confirming that no ZnO or other secondary phases formed during cycling. The electrodes displayed the characteristic reflections of hexagonal Zn, namely the (100), (002), and (101) planes. In the pristine $Zn(TfO)_2$ electrolyte, the diffraction pattern was dominated by the (101) reflection, while the (002) basal peak appeared relatively weak. This orientation preference toward the higher-energy (101) plane is typically associated with kinetically driven growth, rougher surface morphologies, and an increased likelihood of dendritic structures [41,42]. With the incorporation of EMImTfO, a distinct reorientation was observed, as the (002) basal reflection became the most prominent peak. Given that the (002) plane is the most densely packed and lowest in surface energy in the hcp Zn lattice, its dominance indicates a transition to thermodynamically favoured, layered deposition that promotes surface uniformity and suppresses dendrite growth as observed from the SEM. The subsequent addition of EMImI also promoted preferential growth along the (002) basal plane.

3.3. Characterisation of the graphene electrode

Graphene electrode was characterised using Raman spectroscopy and XPS. Fig. 3a shows the Raman spectrum of graphene on a CP electrode. Raman spectrum of graphene electrode shows a D band at 1327 cm^{-1}, associated with defect-activated double resonance scattering, and a G band at 1555 cm^{-1}, arising from the in-plane vibrational mode of sp^2 carbon atoms, which are lower than the typical values reported in the literature (~1345 and 1580 cm^{-1}) [43]. This shift may be due to some oxidation of graphene along with the interactions of PVDF and carbon black with graphene. An additional peak appears at 2685 cm^{-1}, which is generally attributed to the 2D band of multi-layer graphene (Fig. 3a) [44]. The intensity ratio ($I_D/I_G = 0.527$) with a small 2D peak indicates a moderate level of defects or disorder within the graphene structure. Elemental composition and electronic environment of elements were investigated by XPS. A strong C 1 s peak was observed around 284.5 eV, originating from the carbon-rich components. The O 1 s peak appeared at 533 eV, which originates from minor oxidation of graphene. Additionally, a clear F 1 s peak was observed at 688 eV, which is attributed to the presence of PVDF, confirming the incorporation of the fluorine-containing polymer binder in the graphene composition (Fig. 3b). The high-resolution analysis of C 1 s region shown in Fig. 3c can be deconvoluted to five peaks and were assigned to C-C(C=C), C—O (C—N), C═O, O-C=O, and C—F, respectively [45,46]. Additionally, the high-resolution O 1 s spectrum (Fig. 3d) exhibits two peaks at 531.6 and 533 eV, which can be attributed to C═O and C-OH/C-O-C, respectively [45].

3.4. ZIC performance of graphene electrode

Fig. 4a-c shows the cyclic voltammetry curves of the graphene cathode in different electrolytes. In an aqueous electrolyte of 2 M Zn $(TfO)_2$, as depicted in Fig. 4a, all of the CV curves display a reduction process around 0.9 V and an oxidation process at 1.1 V. These peaks are related to the Zn-ion interaction with graphene. Additionally, the large area of the CV curves is attributed to the capacitive behaviour of graphene. CV profiles of IL and redox additives were compared at different scan rates in Fig. 4b and c, respectively. The IL-added $Zn(TfO)_2$ electrolyte shows the quasi-rectangular shape, supporting the capacitive behaviour of ZIC. However, the area under the CV curve is much smaller than that of the aqueous electrolyte, implying a considerable decrease in the capacitive process. In contrast, well-defined cathodic and anodic peaks were observed with EMImI additive to electrolyte as the scan rates increased, due to the combined influence of capacitive and diffusion-controlled processes [12]. A reduction peak at around 1.1 V and an oxidation peak at 1.2 V are observed which can be associated with Zn interaction with graphene along with I redox reaction. Anodic peak potential, E_a, and cathodic peak potential, E_c, differ very slightly (ΔE = 100 mV), indicating the mixed kinetic behaviour at the interface of graphene and the electrolyte. To determine the optimum concentrations of the IL and redox-active species, CV and GCD measurements were performed by varying the concentrations of EMImTfO (1.33–4 M) and EMImI (50–200 mM) to a 2 M $Zn(TfO)_2$ solution (Figs. S2-S9). It was observed that adding IL or the redox species individually did not show a significant increase in capacity. Moreover, the capacity decreased much more rapidly with increasing the current density compared to the electrolyte containing both IL and the redox species. The synergistic enhancements observed in the combined system are most likely due to EMImTfO, which stabilizes the Zn^{2+} coordination environment, suppresses dendrite formation, and mitigates side reactions, together with EMImI, a redox-active species that enhances charge transfer and improves the reversibility of Zn plating/stripping.

The capacitive contribution to the overall capacity was determined by plotting the logarithm of the current (at a specific voltage) against the logarithm of the scan rates, using the equation $i=av^b$, where a is a constant and b is a value ranging from 0.5 (indicating diffusion-

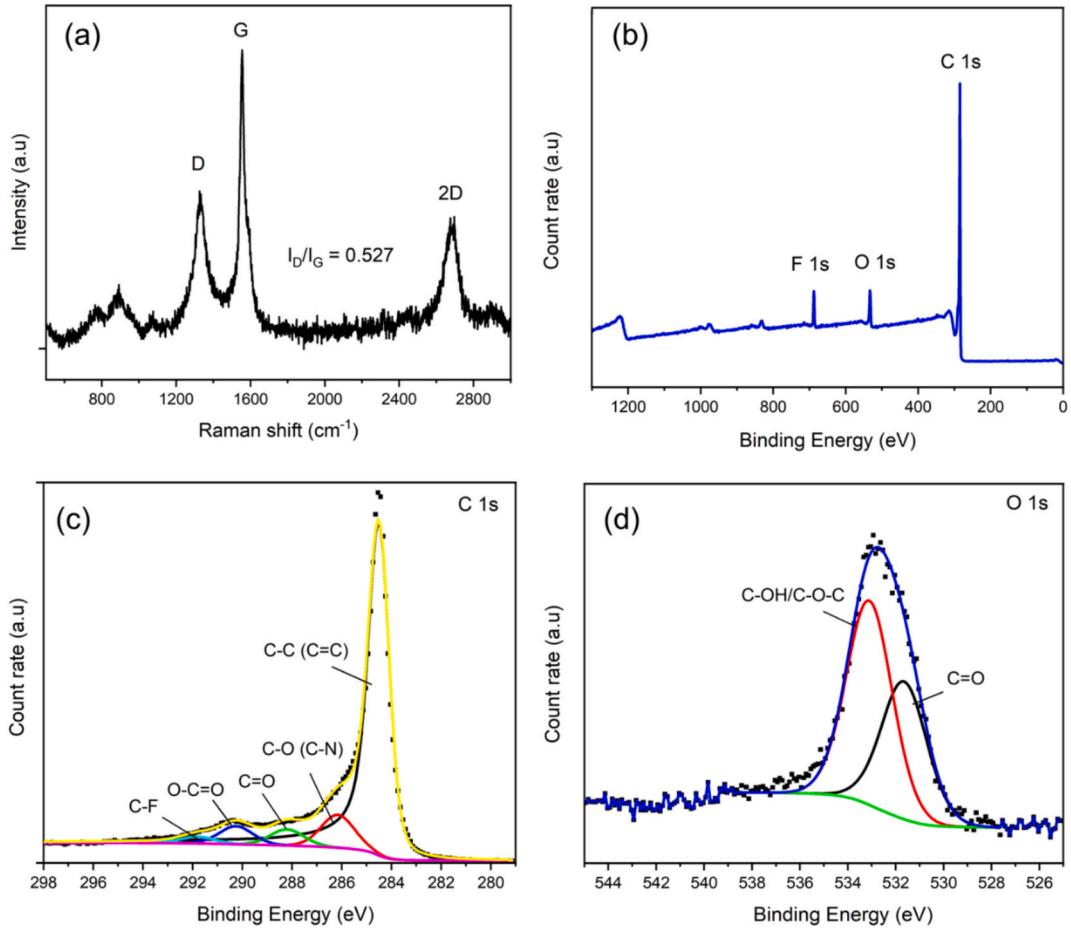

Fig. 3. a) Raman spectrum; b) XPS survey scan, high resolution c) C 1 s and d) O 1 s of graphene electrode.

controlled contribution) to 1 (indicating capacitive contribution) [47–49]. The current was selected at the peak potentials of 1.13 V and 1.23 V for the cathodic and anodic peaks, respectively. As seen in Fig. 4d, the value of b was found to be 0.60 for the cathodic process, indicating a predominantly diffusion-controlled process, and 0.81 for the anodic processes, indicating the presence of a capacitive process. In Fig. 4e, the bar chart displays the capacitive process contribution to the total capacity. It shows that as the scan rate rises, the capacitive contribution increases from 45.75 % at 1 mV s^{-1} to 65.35 % at 5 mV s^{-1}. This increase in capacitance with the scan rate is consistent with previous observations [4,12].

To investigate the effect of electrolytes, charge/discharge studies were performed in a bespoke cell. Fig. 5a-c presents the charge/discharge cycle at different current densities (0.5–5 A g^{-1}) for the three different electrolytes. It is observed from Fig. 5a and b, graphene electrode exhibits a capacity of 82 and 96 mAh g^{-1} at a current density of 0.5 A g^{-1} in 2 M $Zn(TfO)_2$ and in 1.33 M EMImTfO +2 M $Zn(TfO)_2$ electrolytes, respectively. However, a capacity of 182 mAh g^{-1} can be achieved at the same current density in 1.33 M EMImTfO +50 mM EMImI +2 M $Zn(TfO)_2$. It is noteworthy that even at a current density of 5 A g^{-1}, the capacity remains nearly 100 mAh g^{-1}, and the decrease in capacity with increasing current density is lower than other electrolytes (Fig. 5c). The low coulombic efficiency observed in Fig. 5c can be attributed to slower diffusion of iodides at the electrode/electrolyte interface due to the presence of ionic liquid in the double layer [50].

The cyclic test was performed at 5 A g^{-1} in the mixed electrolyte (Fig. 5d). The increase in capacity during the initial 200 cycles can be attributed to the activation process of the graphene electrode in the mixed ionic liquid aqueous electrolyte [13]. With cycling, more I^- may be physically adsorbed on the surface of graphene. Subsequently, the capacity slowly decreased to 92 mAh g^{-1} at the end of the 1400 cycles, corresponding to a capacity retention of 92 %, while remaining with a high coulombic efficiency over 97 % (Fig. 5d). In comparison, the cycling stability conducted in the electrolyte 2 M $Zn(TfO)_2$/EMImI (Fig. S10) showed a rapid capacity decay indicating poor cycling stability in the absence of EMImTfO and highlights the synergistic effect of the mixed electrolyte.

The Ragone plot (Fig. 5e) shows an energy density of 154.2 Wh kg^{-1} and the power density of 0.4 kW kg^{-1} that can be achieved at a current density of 0.5 A g^{-1}, which is approximately twice that of the EMImI-free system, indicating the significant contribution of EMImI to enhancing the overall energy capability (Fig. 5e). To further highlight the electrochemical performance of the graphene electrode, the energy density and power density were compared with recently reported carbon-based cathode materials in Fig. 5f [51–57]. It clearly demonstrates the competitive electrochemical performance when compared to recent literature, supporting its potential application in aqueous ZICs.

3.5. *Ex situ Raman spectroscopy and XPS studies*

Raman spectroscopy was employed to investigate the structural changes in graphene electrode during charge/discharge cycling in different electrolyte compositions. Fig. 6a-c compares the change of Raman shift in graphene at discharge up to 0.5 V and charge up to 1.6 V in three different electrolytes. Initially, the D and G bands appeared at 1327 and 1555 cm^{-1}, respectively. Upon discharging to 0.5 V in all electrolytes, both the D and G bands exhibited a blueshift, accompanied by band broadening. This indicates structural modification, which may

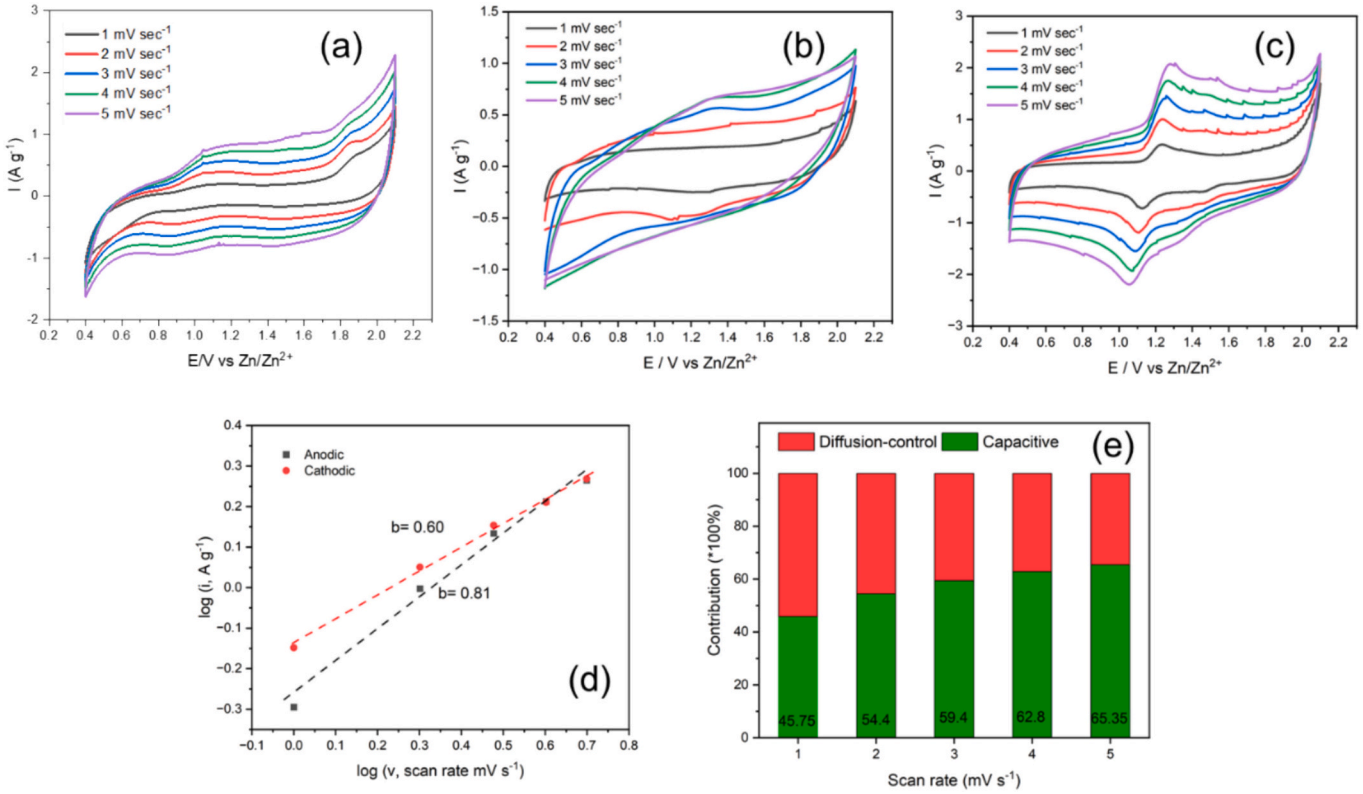

Fig. 4. CV curves of graphene electrode in (a) 2 M $Zn(TfO)_2$ aqueous electrolyte, (b) 1.33 M EMImTfO in 2 M $Zn(TfO)_2$, (c) 1.33 M EMImTfO and 50 mM EMImI in 2 M $Zn(TfO)_2$, (d) relationship between log i and log v plots for the cathodic and anodic sweeps of CV, e) diagram of the capacitive contribution to the total capacity at different scan rates in 1.33 M EMImTfO and 50 mM EMImI in 2 M $Zn(TfO)_2$.

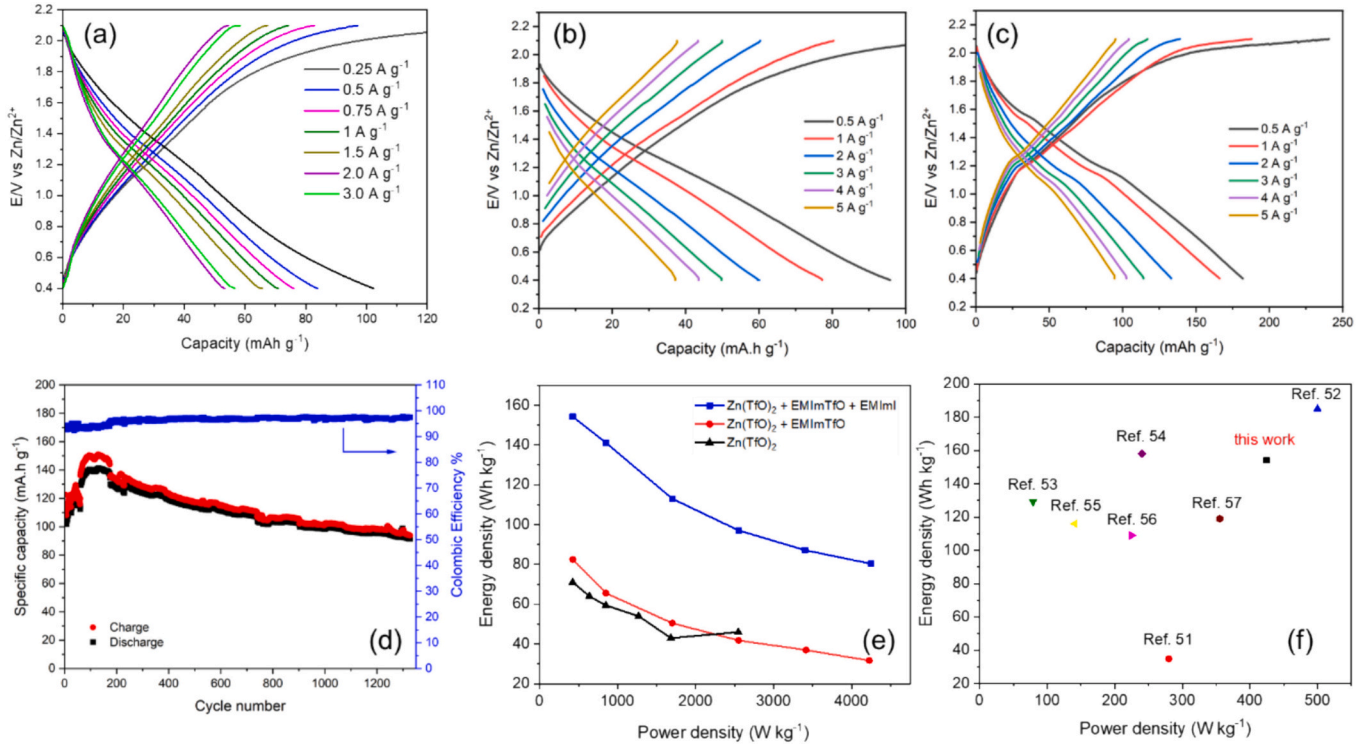

Fig. 5. Charge/discharge cycle of Zn/graphene at 0.5–5 A g^{-1} in a) 2 M $Zn(TfO)_2$ aqueous electrolyte, (b) 1.33 M EMImTfO in 2 M $Zn(TfO)_2$, (c) 1.33 M EMImTfO and 50 mM EMImI in 2 M $Zn(TfO)_2$ electrolytes, d) change in specific capacity with cycle number of mixed electrolyte at 5 A g^{-1}, e) Comparison of the Ragone plot of graphene electrode with three electrolyte systems, and f) Comparison of the electrochemical performances of graphene electrode with recently reported carbon-based cathode materials.

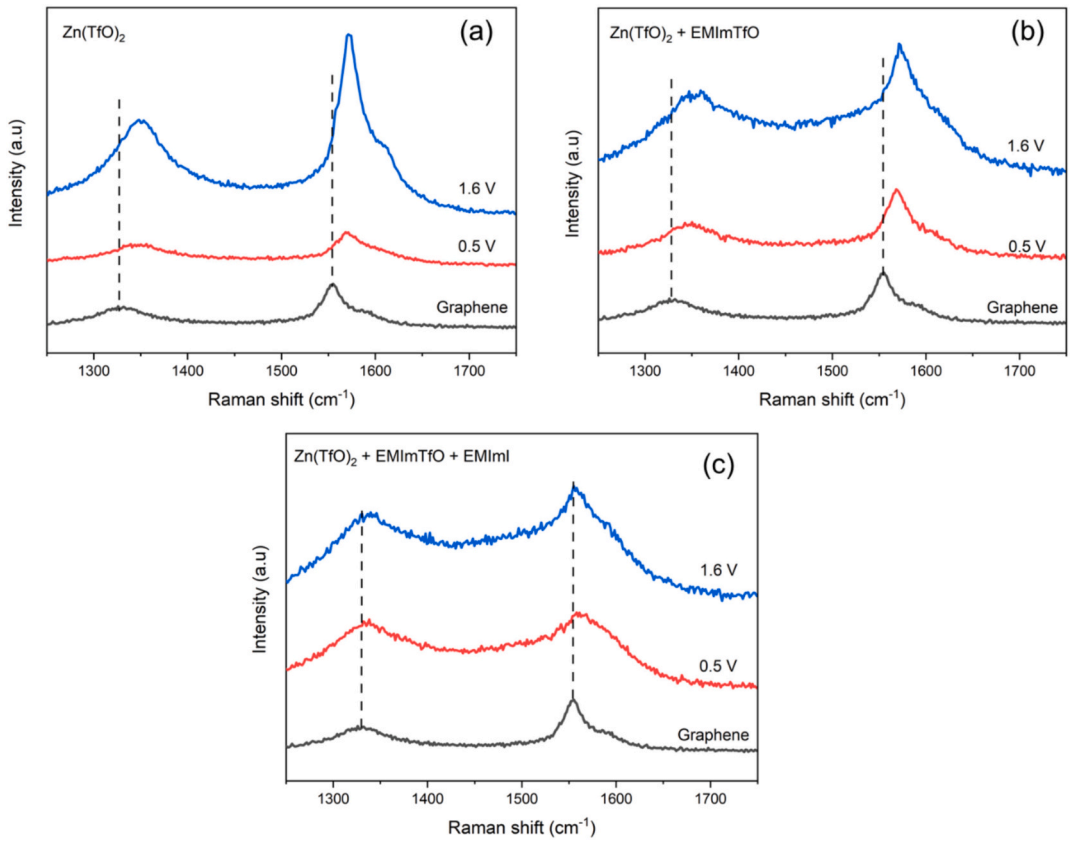

Fig. 6. Comparison of Raman spectra of graphene electrode after discharging and charging in a) $Zn(TfO)_2$ b) $Zn(TfO)_2$ + EMImTfO, c) $Zn(TfO)_2$ + EMImTfO + EMImI.

be attributed to the Zn^{2+} interaction with graphene. This finding is consistent with the literature [58]. Upon recharging to 1.6 V, the G band in the EMImI-containing system shifted back to 1555 cm^{-1} (Fig. 6c), while in the other electrolytes it remained in the same position (1571 cm^{-1}) (Fig. 6a,b), indicating enhanced structural reversibility with EMImI (Fig. 6c). To further understand the Zn interaction with graphene in 2 M $Zn(TfO)_2$ + 1.33 M EMImTfO +50 mM EMImI, Raman shifts in graphene electrode were investigated at various discharge/charge potentials (Fig. S11a). No significant changes were observed up to 0.9 V discharging. Below 0.9 V, both D and G bands exhibited noticeable broadening, accompanied by a slight blue shift in the G band. Upon further charging, this shift was found to be reversible, with the G band returning to its original position. This behaviour can be attributed to the Zn^{2+} and iodine interaction within the graphene structure. In ex situ Raman analysis, the observed increase in the I_D/I_G ratio at various discharge/charge potentials indicate the adsorption of cations onto the electrode surface [58]. The rising I_D/I_G ratio suggests the interaction with Zn/I with graphene, which disrupt the sp^2 carbon lattice

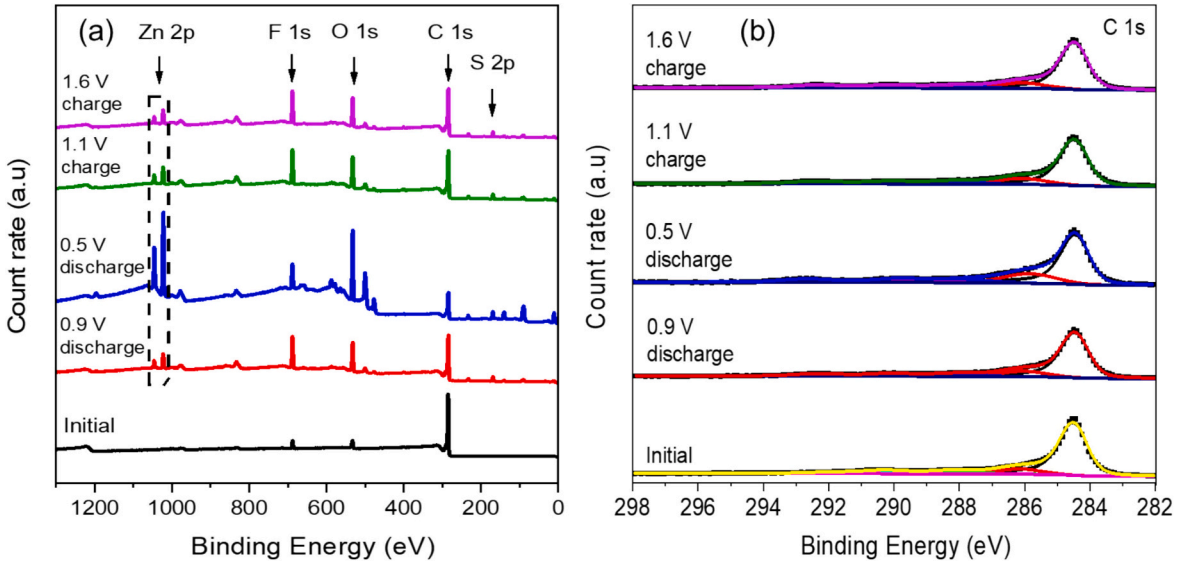

Fig. 7. (a) Survey spectra and (b) high-resolution C 1 s spectra of graphene electrode after various discharge-charge potentials in 2 M aqueous $Zn(TfO)_2$ electrolyte.

(Fig. S11b). The results are consistent with prior studies showing that ion intercalation significantly affects the D and G bands in graphene [59,60]. After long-term cycling in $Zn(TfO)_2$ + EMImTfO + EMImI electrolyte, the Raman spectra gradually changed. After 750 cycles, the D and G bands shifted to 1351 and 1570 cm^{-1}, indicating interaction with Zn/I. After 1400 cycles, D band shifted to 1337 cm^{-1} while the G band remained at 1569 cm^{-1}, suggesting that defects formed in graphene might have saturated (Fig. S11c).

XPS was also performed to investigate the changes in the graphene electrode after cycling at various discharge and charge potentials. Fig. 7 compares the XPS of pristine graphene electrode with those obtained after discharging to 0.5 V and charging to 1.6 V in 2 M $Zn(TfO)_2$ electrolyte. From the survey spectra in Fig. 7a, the graphene electrode exhibits C, O and F signals. The F signal originates from the PVDF binder. Upon discharging to 0.9 and 0.5 V, additional peaks appear at 168 eV and > 1000 eV appear. These are attributed to the S 2p signal from TFO^- anion in the electrolyte, and Zn in graphene matrix, respectively. During discharging, the intensity of the C 1 s signal decreased. This suppression of the C 1 s peak suggests the presence of electrolyte remaining strongly adsorbed to the surface, which effectively obscures the underlying graphene [61]. During charging to 1.1 V and 1.6 V, Zn signals decrease, reflecting Zn deintercalation. The detailed spectra of Zn 2p in Fig. S12 display the changes of Zn during the discharging and charging process. The high-resolution spectra of C 1 s in Fig. 7b reveal changes in the graphene electrode during cycling at various discharge and charge potentials. C—O and O-C=O peaks shifted from 288.2 and 290.3 to 287.8 eV and to 289.9 eV binding energies after discharge, respectively, indicating surface reduction and Zn^{2+} interaction. Upon subsequent charging, this peak partially returned to its original position. The C—F peak shifted to a higher binding energy and exhibited an increase in intensity, which suggests enhanced interaction between TfO^- anion.

The survey XPS spectra of the graphene electrode cycled in $Zn(TfO)_2$ with EMImTfO revealed notable changes compared to the pristine state, indicating interfacial reactions driven by both Zn ion intercalation and ionic liquid interactions. In addition to the original C, O, F and S peaks, new peak corresponding to N 1 s (400 eV) were observed during discharging and charging, which can be related to adsorption of the $EMIm^+$ cation. The intensities of Zn 2p peaks (1024 and 1047 eV) significantly increased on discharging and decreased during the charge process, indicating the intercalation/deintercalation of Zn^{2+} ions (Fig. 8a). The detailed spectra of Zn 2p in Fig. S13 display the changes of Zn during the discharging and charging process. High resolution C 1 s and N 1 s are shown in Fig. 8 b-c, respectively. After full discharge, the O-C=O, C—O, and C—F peaks shift by 0.6/0.7 eV, and the intensity of C—F peak increases, resembling the behaviour observed in the aqueous electrolyte in Fig. 7b. These shifts can be related to Zn intercalation. The high-resolution N 1 s spectrum of graphene electrode during discharging and charging exhibits two peaks at 400 and 401.6 eV, indicating the presence of pyrrolic and graphitic nitrogen, respectively (Fig. 8c) [45]. These peaks, which were not present in the pristine graphene electrode, emerged during the discharge and charging processes. The absence of any noticeable shifts in their positions or changes in their intensities suggests that they originate from adsorption of the $EMIm^+$ cation present in the electrolyte.

XPS analysis of the graphene electrode cycled in $Zn(TfO)_2$ electrolyte containing both EMImTfO and EMImI shown in Fig. 9. The survey spectra display the peaks of S 2p (168 eV), N 1 s (402 eV), F 1 s (689.6 eV), and Zn 2p (1022 and 1046.4 eV) after discharge, indicating Zn^{2+} intercalation and the adsorption of ionic liquid. The Zn signal reached maximum intensity at 0.5 V discharge and decreased during charging, suggesting reversible Zn intercalation/deintercalation behaviour (Fig. 9a). The detailed spectra of Zn 2p in Fig. S14 display the changes of Zn during the discharging and charging process. The high-resolution C 1 s spectra exhibited five previously identified characteristic peaks. Similar behaviour was also observed in the other two electrolytes (Fig. 9b). The appearance of two N1s peaks at 399.85 eV and 401.58 eV in all cycling stages suggests that they originate from adsorption of the $EMIm^+$ cation present in the electrolyte (Fig. 9c).

Thus, based on the XPS analysis of graphene electrodes cycled in three electrolytes, the progressive impact of ionic liquid and redox-active species additive on structure and Zn intercalation/deintercalation process is evident which is responsible for improving the capacity in ZIC.

4. Conclusion

In summary, we have investigated the effect of both IL and redox species on the structural and electrochemical properties of the graphene electrode as a cathode material for ZIC. The incorporation of EMImTfO and EMImI into the $Zn(TfO)_2$ aqueous electrolyte significantly enhances the electrochemical performance of graphene electrode by nearly doubling the capacity of the electrode and improving capacity retention at high current densities. However, individual addition of EMImTfO or EMImI to the electrolyte did not significantly enhance the capacity. The synergistic effect of ionic liquid and redox-active species not only boosts energy storage capabilities but also effectively suppresses zinc dendrite formation and HER. Graphene electrode delivers capacities of 82, 96 mAh g^{-1} and 182 mAh g^{-1} at 0.5 A g^{-1} in $Zn(TfO)_2$ and $Zn(TfO)_2$/

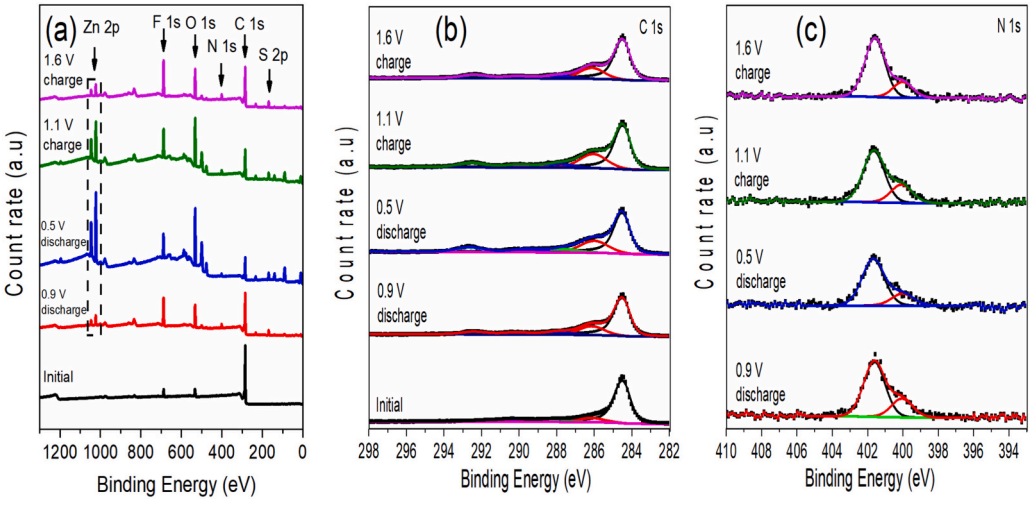

Fig. 8. (a) Survey spectra, (b) high-resolution C 1 s spectra, and (c) high-resolution N 1 s spectra of graphene electrode after various discharge-charge potential in 2 M $Zn(TfO)_2$ + 1.33 M EMImTfO electrolyte.

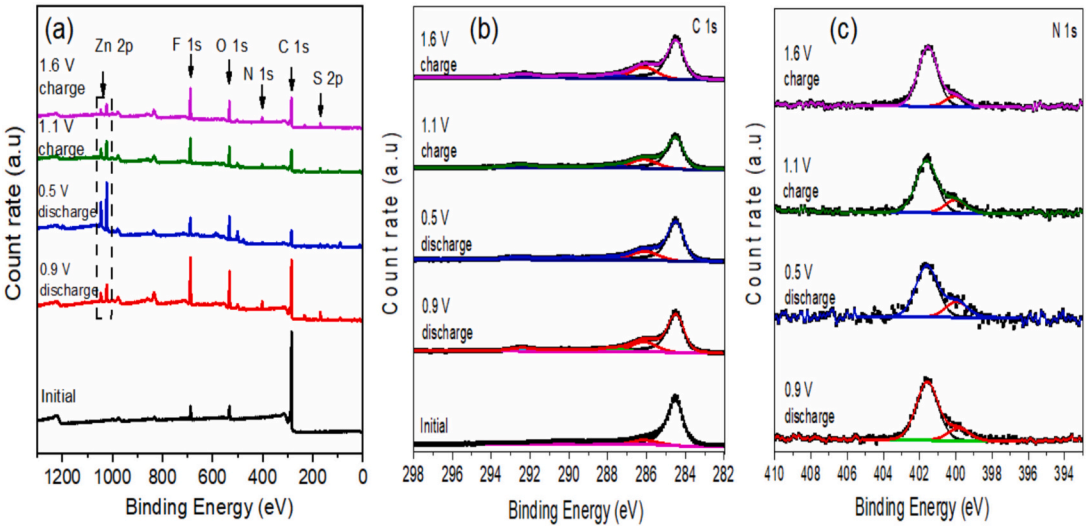

Fig. 9. (a) Survey spectra, (b) high-resolution C 1 s spectra, and (c) high-resolution N 1 s spectra of graphene electrode after various discharge-charge potentials in 2 M $Zn(TfO)_2$ + 1.33 M EMImTfO +50 mM EMImI electrolyte.

EMImTfO and $Zn(TfO)_2$/ EMImTfO/ EMImI electrolytes, respectively. Moreover, even at a current density of 5 A g^{-1}, the capacity remains nearly 100 mAh g^{-1} in the redox active electrolyte. These results demonstrate a viable and scalable approach to designing advanced redox-active electrolytes, facilitating the way for durable, high-performance, and sustainable energy storage devices.

CRediT authorship contribution statement

Emine Kapancik Ulker: Writing – original draft, Methodology, Investigation, Formal analysis, Data curation. **Kazem Mohammadzadeh:** Writing – original draft, Methodology, Investigation, Formal analysis, Data curation. **Abhishek Lahiri:** Writing – review & editing, Supervision, Funding acquisition, Conceptualization.

Declaration of competing interest

The authors declare the following financial interests/personal relationships which may be considered as potential competing interests: Abhishek Lahiri reports financial support was provided by Engineering and Physical Sciences Research Council. If there are other authors, they declare that they have no known competing financial interests or personal relationships that could have appeared to influence the work reported in this paper.

Acknowledgements

This research was funded, in whole by EPSRC, EP/W015129/1. Emine Kapancik Ulker thanks the Scientific and Technological Research Council of Turkey (TUBITAK) for the support (Project No: 1059B192301430). We thank Dr Shaoliang Guan, Maxwell centre, The University of Cambridge for XPS measurements.

Appendix A. Supplementary data

Supplementary data to this article can be found online at https://doi.org/10.1016/j.est.2025.119828.

Data availability

Lahiri, Abhishek (2025). Zn ion capacitors in aprotic ionic liquids. Brunel University London. Dataset. https://brunel.figshare.com/articles/dataset/_/30157126

References

[1] L. Hu, L. Bo, N. Wang, M. Sun, X. Ren, Z. Li, C. Jia, Tuning the porous graphene interlayer structure for compact energy storage towards high volumetric performance of Zn-ion capacitor, Chem. Eng. J. 479 (2024), https://doi.org/10.1016/j.cej.2023.147570.
[2] H. Li, Y. Yu, T. Wang, Y. Zhang, J. You, F. Hu, K. Zhu, Zinc-ion hybrid capacitors: Electrode material design and electrochemical storage mechanism, J. Power Sources 610 (2024), https://doi.org/10.1016/j.jpowsour.2024.234638.
[3] L. Wang, M. Peng, J. Chen, X. Tang, L. Li, T. Hu, K. Yuan, Y. Chen, High energy and power zinc ion capacitors: A dual-ion adsorption and reversible chemical adsorption coupling mechanism, ACS Nano 16 (2022) 2877–2888.
[4] A. Lahiri, L. Yang, G. Li, F. Endres, Mechanism of Zn-ion intercalation-Deintercalation in a Zn– Polypyrrole secondary battery in aqueous and bio-ionic liquid electrolytes, ACS Appl. Mater. Interfaces 11 (2019) 45098–45107.
[5] Z. Ye, Z. Cao, M.O. Lam Chee, P. Dong, P.M. Ajayan, J. Shen, M. Ye, Advances in Zn-ion batteries via regulating liquid electrolyte, Energy Storage Mater. 32 (2020) 290–305, https://doi.org/10.1016/j.ensm.2020.07.011.
[6] X. Gao, H. Dong, C.J. Carmalt, G. He, Recent advances of aqueous electrolytes for zinc-ion batteries to mitigate side reactions: A review, ChemElectroChem 10 (2023), https://doi.org/10.1002/celc.202300200.
[7] L. Tan, Y. Lin, Z. Zhong, G. Yang, C. Wang, Recent advances in hybrid aqueous-organic electrolytes for zinc-ion batteries, Chem. Eng. J. 502 (2024), https://doi.org/10.1016/j.cej.2024.157927.
[8] Y. Bai, D. Deng, J. Wang, Y. Wang, Y. Chen, H. Zheng, M. Liu, X. Zheng, J. Jiang, H. Zheng, M. Yi, W. Li, G. Fang, D. Wang, Y. Lei, Inhibited passivation by bioinspired cell membrane Zn Interface for Zn–air batteries with extended temperature adaptability, Adv. Mater. 36 (2024) 2411404, https://doi.org/10.1002/adma.202411404.
[9] W. Zhou, M. Zhang, X. Kong, W. Huang, Q. Zhang, Recent advance in ionic-liquid-based electrolytes for rechargeable metal-ion batteries, Adv. Sci. 8 (2021), https://doi.org/10.1002/advs.202004490.
[10] J. Chen, W. Zhou, Y. Quan, B. Liu, M. Yang, M. Chen, X. Han, X. Xu, P. Zhang, S. Shi, Ionic liquid additive enabling anti-freezing aqueous electrolyte and dendrite-free Zn metal electrode with organic/inorganic hybrid solid electrolyte interphase layer, Energy Storage Mater. 53 (2022) 629–637, https://doi.org/10.1016/j.ensm.2022.10.004.
[11] Z. Zhao, J. Lai, D.T. Ho, Y. Lei, J. Yin, L. Chen, U. Schwingenschlögl, H. N. Alshareef, A Novel "Water-in-ionic liquid" Electrolyte for Zn Metal Batteries, ACS Energy Lett. 8 (2023) 608–618, https://doi.org/10.1021/acsenergylett.2c02520.
[12] X. Gan, C. Zhang, X. Ye, L. Qie, K. Shi, Unveiling the potential of redox electrolyte additives in enhancing interfacial stability for Zn-ion hybrid capacitors, Energy Storage Mater. 65 (2024), https://doi.org/10.1016/j.ensm.2024.103175.
[13] L. Wei, Y. Chen, Z. Huang, S. Zheng, X. Guo, Redox-enhanced zinc-ion hybrid capacitors with high energy density enabled by high-voltage active aqueous electrolytes based on low salt concentration, Energy Storage Mater. 58 (2023) 30–39, https://doi.org/10.1016/j.ensm.2023.03.015.
[14] S.E. Chun, B. Evanko, X. Wang, D. Vonlanthen, X. Ji, G.D. Stucky, S.W. Boettcher, Design of aqueous redox-enhanced electrochemical capacitors with high specific energies and slow self-discharge, Nat. Commun. 6 (2015), https://doi.org/10.1038/ncomms8818.
[15] L. Han, H. Huang, J. Li, X. Zhang, Z. Yang, M. Xu, L. Pan, A novel redox bromide-ion additive hydrogel electrolyte for flexible Zn-ion hybrid supercapacitors with boosted energy density and controllable zinc deposition, J. Mater. Chem. A 8 (2020) 15042–15050, https://doi.org/10.1039/D0TA03547E.

[16] F. Yu, C. Zhang, F. Wang, Y. Gu, P. Zhang, E.R. Waclawik, A. Du, K. (Ken) Ostrikov, H. Wang, A zinc bromine "supercapattery" system combining triple functions of capacitive, pseudocapacitive and battery-type charge storage, Mater. Horiz. 7 (2020) 495–503, https://doi.org/10.1039/C9MH01353A.

[17] L. Han, H. Huang, J. Li, Z. Yang, X. Zhang, D. Zhang, X. Liu, M. Xu, L. Pan, Novel zinc–iodine hybrid supercapacitors with a redox iodide ion electrolyte and B, N dual-doped carbon electrode exhibit boosted energy density, J. Mater. Chem. A 7 (2019) 24400–24407, https://doi.org/10.1039/C9TA07196B.

[18] J. Wang, M. Chen, D. Shao, I. Zhitomirsky, K. Shi, Zn-ion hybrid capacitors utilizing redox electrolytes derived from naphthoquinone molecules, Mater. Today Energy 51 (2025) 101893, https://doi.org/10.1016/j.mtener.2025.101893.

[19] M. Chen, L. Gong, I. Zhitomirsky, K. Shi, Unraveling the dynamic transformation of azobenzene-driven redox electrolytes for Zn-ion hybrid capacitors, Energy Environ. Sci. 18 (2025) 4460–4469, https://doi.org/10.1039/d4ee05696e.

[20] M. Chen, R. Chen, I. Zhitomirsky, G. He, K. Shi, Redox-active molecules for aqueous electrolytes of energy storage devices: A review on fundamental aspects, current progress, and prospects, Mater. Sci. Eng. R. Rep. 161 (2024), https://doi.org/10.1016/j.mser.2024.100865.

[21] Y. Lu, Z. Li, Z. Bai, H. Mi, C. Ji, H. Pang, C. Yu, J. Qiu, High energy-power Zn-ion hybrid supercapacitors enabled by layered B/N co-doped carbon cathode, Nano Energy 66 (2019), https://doi.org/10.1016/j.nanoen.2019.104132.

[22] J. Yin, W. Zhang, W. Wang, N.A. Alhebshi, N. Salah, H.N. Alshareef, Electrochemical zinc ion capacitors enhanced by redox reactions of porous carbon cathodes, Adv. Energy Mater. 10 (2020), https://doi.org/10.1002/aenm.202001705.

[23] S. Yamazaki, T. Ito, M. Yamagata, M. Ishikawa, Non-aqueous electrochemical capacitor utilizing electrolytic redox reactions of bromide species in ionic liquid, Electrochim. Acta (2012) 294–297, https://doi.org/10.1016/j.electacta.2012.01.031.

[24] T. Tooming, T. Thomberg, L. Siinor, K. Tõnurist, A. Jänes, E. Lust, A type high capacitance supercapacitor based on mixed room temperature ionic liquids containing specifically adsorbed iodide anions, J. Electrochem. Soc. 161 (2014) A222–A227, https://doi.org/10.1149/2.014403jes.

[25] D.-J. You, Z. Yin, Y. Ahn, S.-H. Lee, J. Yoo, Y.S. Kim, Redox-active ionic liquid electrolyte with multi energy storage mechanism for high energy density supercapacitor, RSC Adv. 7 (2017) 55702–55708, https://doi.org/10.1039/C7RA10772B.

[26] L. Huang, J. Gu, B. Wang, W. He, S. Xiao, J. Liao, Z. Chang, Z. Jia, S. Zhai, Y. He, H. Liu, F. Zhang, W. Feng, Surface pyrolysis towards graphite heterojunctions for aqueous zinc-ion capacitor, Chem. Eng. J. 513 (2025), https://doi.org/10.1016/j.cej.2025.163094.

[27] L. Huang, Z. Gu, J. Gu, F. Zhang, J. Zhuang, Q. Ma, T. Zhang, J. Li, H. Liu, W. Feng, Green synthesis of sodium pyrithione salt-activated biomass-derived carbon for aqueous zinc-ion capacitors, Green Chem. 26 (2024) 10196–10204, https://doi.org/10.1039/d4gc02429j.

[28] L. Huang, Z. Gu, W. He, K. Shi, L. Peng, Z. Sheng, F. Zhang, W. Feng, H. Liu, Solvothermal synthesis and pyrolysis toward heteroatom-doped carbon microspheres for zinc-ion hybrid capacitors, Small 20 (2024) 1–9, https://doi.org/10.1002/smll.202308788.

[29] Y. Wang, S. Sun, X. Wu, H. Liang, W. Zhang, Status and opportunities of zinc ion hybrid capacitors: Focus on carbon materials, current collectors, and separators, Nano Micro Lett. 15 (2023), https://doi.org/10.1007/s40820-023-01065-x.

[30] L. Yu, J. Li, N. Ahmad, X. He, G. Wan, R. Liu, X. Ma, J. Liang, Z. Jiang, G. Zhang, Recent progress on carbon materials for emerging zinc-ion hybrid capacitors, J. Mater. Chem. A 12 (2024) 9400–9420, https://doi.org/10.1039/d4ta00252k.

[31] Y. Zhu, X. Ye, H. Jiang, J. Xia, Z. Yue, L. Wang, Z. Wan, C. Jia, X. Yao, Controlled swelling of graphene films towards hierarchical structures for supercapacitor electrodes, J. Power Sources 453 (2020), https://doi.org/10.1016/j.jpowsour.2020.227851.

[32] G.-H. An, Ultrafast long-life zinc-ion hybrid supercapacitors constructed from mesoporous structured activated carbon, Appl. Surf. Sci. 530 (2020) 147220, https://doi.org/10.1016/j.apsusc.2020.147220.

[33] L. Dong, X. Ma, Y. Li, L. Zhao, W. Liu, J. Cheng, C. Xu, B. Li, Q.-H. Yang, F. Kang, Extremely safe, high-rate and ultralong-life zinc-ion hybrid supercapacitors, Energy Storage Mater. 13 (2018) 96–102, https://doi.org/10.1016/j.ensm.2018.01.003.

[34] Y. Shao, Z. Sun, Z. Tian, S. Li, G. Wu, M. Wang, X. Tong, F. Shen, Z. Xia, V. Tung, J. Sun, Y. Shao, Regulating oxygen substituents with optimized redox activity in chemically reduced graphene oxide for aqueous Zn-ion hybrid capacitor, Adv. Funct. Mater. 31 (2021), https://doi.org/10.1002/adfm.202007843.

[35] X. Li, Y. Li, X. Zhao, F. Kang, L. Dong, Elucidating the charge storage mechanism of high-performance vertical graphene cathodes for zinc-ion hybrid supercapacitors, Energy Storage Mater. 53 (2022) 505–513, https://doi.org/10.1016/j.ensm.2022.09.023.

[36] C.M.S. Prasanna, S.A. Suthanthiraraj, Electrical, structural, and morphological studies of honeycomb-like microporous zinc-ion conducting poly (vinyl chloride)/poly (ethyl methacrylate) blend-based polymer electrolytes, Ionics (Kiel) 22 (2016) 389–404, https://doi.org/10.1007/s11581-015-1546-4.

[37] S.A. Suthanthiraraj, R. Kumar, B.J. Paul, FT-IR spectroscopic investigation of ionic interactions in PPG 4000: AgCF3SO3 polymer electrolyte, Spectrochim. Acta Part A Mol. Biomol. Spectrosc. 71 (2009) 2012–2015, https://doi.org/10.1016/j.saa.2008.07.040.

[38] Z. Liu, S.Z. El Abedin, F. Endres, Raman and FTIR spectroscopic studies of 1-Ethyl-3-methylimidazolium Trifluoromethylsulfonate, its mixtures with water and the solvation of zinc ions, ChemPhysChem 16 (2015) 970–977, https://doi.org/10.1002/cphc.201402831.

[39] S. Bai, Z. Huang, G. Liang, R. Yang, D. Liu, W. Wen, X. Jin, C. Zhi, X. Wang, Electrolyte additives for stable Zn anodes, Adv. Sci. 11 (2024), https://doi.org/10.1002/advs.202304549.

[40] X. Sen Lin, Z.R. Wang, L.H. Ge, J.W. Xu, W.Q. Ma, M.M. Ren, W.L. Liu, J.S. Yao, C. Bin Zhang, Electrolyte modification for long-life Zn ion batteries: Achieved by methanol additive, ChemElectroChem 9 (2022) e202101724, https://doi.org/10.1002/celc.202101724.

[41] S. Wu, Z. Hu, P. He, L. Ren, J. Huang, J. Luo, Crystallographic engineering of Zn anodes for aqueous batteries, EScience 3 (2023) 100120, https://doi.org/10.1016/j.esci.2023.100120.

[42] K. Mohammadzadeh, U.K. Roy, A. Lahiri, Electrochemical and spectroscopic studies of zinc oxide in an eco-friendly deep eutectic solvent for Zn electrodeposition, J. Electrochem. Soc. 172 (2025) 052505, https://doi.org/10.1149/1945-7111/adda79.

[43] Y.J. Kwon, H.S. Park, Y.P. Jeon, Graphite–graphene architecture for Zn-ion hybrid supercapacitor electrodes, Carbon Lett. 32 (2022) 1307–1313, https://doi.org/10.1007/s42823-022-00362-6.

[44] A.G. Güell, N. Ebejer, M.E. Snowden, J.V. Macpherson, P.R. Unwin, Structural correlations in heterogeneous Electron transfer at monolayer and multilayer graphene electrodes, J. Am. Chem. Soc. 134 (2012) 7258–7261, https://doi.org/10.1021/ja3014902.

[45] A. Patrike, K. Suresh, M. Wahid, V. Chaturvedi, M.V. Shelke, Ice-colloidal templated carbon host for highly efficient, dendrite free Li metal anode, Carbon N. Y. 179 (2021) 256–265, https://doi.org/10.1016/j.carbon.2021.04.021.

[46] Z. Xing, Z. Ju, Y. Zhao, J. Wan, Y. Zhu, Y. Qiang, Y. Qian, One-pot hydrothermal synthesis of nitrogen-doped graphene as high-performance anode materials for lithium ion batteries, Sci. Rep. 6 (2016) 26146, https://doi.org/10.1038/srep26146.

[47] V. Augustyn, J. Come, M.A. Lowe, J.W. Kim, P.-L. Taberna, S.H. Tolbert, H. D. Abruña, P. Simon, B. Dunn, High-rate electrochemical energy storage through Li + intercalation pseudocapacitance, Nat. Mater. 12 (2013) 518–522, https://doi.org/10.1038/nmat3601.

[48] C. Chen, Y. Wen, X. Hu, X. Ji, M. Yan, L. Mai, P. Hu, B. Shan, Y. Huang, Na+ intercalation pseudocapacitance in graphene-coupled titanium oxide enabling ultra-fast sodium storage and long-term cycling, Nat. Commun. 6 (2015) 6929, https://doi.org/10.1038/ncomms7929.

[49] D. Chao, P. Liang, Z. Chen, L. Bai, H. Shen, X. Liu, X. Xia, Y. Zhao, S.V. Savilov, J. Lin, Z.X. Shen, Pseudocapacitive Na-ion storage boosts high rate and areal capacity of self-branched 2D layered metal chalcogenide Nanoarrays, ACS Nano 10 (2016) 10211–10219, https://doi.org/10.1021/acsnano.6b05566.

[50] M. Vijayakumar, B. Schwenzer, V. Shutthanandan, J. Hu, J. Liu, I.A. Aksay, Elucidating graphene–ionic liquid interfacial region: A combined experimental and computational study, Nano Energy 3 (2014) 152–158, https://doi.org/10.1016/j.nanoen.2012.09.014.

[51] Q. Wang, S. Wang, X. Guo, L. Ruan, N. Wei, Y. Ma, J. Li, M. Wang, W. Li, W. Zeng, MXene-reduced graphene oxide aerogel for aqueous zinc-ion hybrid supercapacitor with ultralong cycle life, Adv. Electron. Mater. 5 (2019) 1900537, https://doi.org/10.1002/aelm.201900537.

[52] S. Brahma, J. Huddleston, E. Kapancik Ulker, A. Lahiri, Enhancing the energy density of Zn-ion capacitors using redox-active choline anthraquinone electrolyte, Batteries Supercaps (2025) e202500406, https://doi.org/10.1002/batt.202500406.

[53] Z. Li, J. Huo, W. Zhao, L. Fan, M. Zheng, S. Guo, Waste cotton fabrics-derived oxygen-rich porous carbon cathode for high-performance zinc-ion capacitors, Mater. Today Commun. 49 (2025) 113969, https://doi.org/10.1016/j.mtcomm.2025.113969.

[54] J. Liu, Z. Khanam, S. Ahmed, T. Wang, H. Wang, S. Song, Flexible antifreeze Zn-ion hybrid supercapacitor based on gel electrolyte with graphene electrodes, ACS Appl. Mater. Interfaces 13 (2021) 16454–16468, https://doi.org/10.1021/acsami.1c02242.

[55] C. Liu, X. Xie, B. Lu, J. Zhou, S. Liang, Electrolyte strategies toward better zinc-ion batteries, ACS Energy Lett. 6 (2021) 1015–1033, https://doi.org/10.1021/acsenergylett.0c02684.

[56] G. Lou, G. Pei, Y. Wu, Y. Lu, Y. Wu, X. Zhu, Y. Pang, Z. Shen, Q. Wu, S. Fu, H. Chen, Combustion conversion of wood to N, O co-doped 2D carbon nanosheets for zinc-ion hybrid supercapacitors, Chem. Eng. J. 413 (2021) 127502, https://doi.org/10.1016/j.cej.2020.127502.

[57] B. Xue, J. Xu, R. Xiao, Ice template-assisting activation strategy to prepare biomass-derived porous carbon cages for high-performance Zn-ion hybrid supercapacitors, Chem. Eng. J. 454 (2023) 140192, https://doi.org/10.1016/j.cej.2022.140192.

[58] X.-T. Yin, E.-M. You, R.-Y. Zhou, L.-H. Zhu, W.-W. Wang, K.-X. Li, D.-Y. Wu, Y. Gu, J.-F. Li, B.-W. Mao, J.-W. Yan, Unraveling the energy storage mechanism in graphene-based nonaqueous electrochemical capacitors by gap-enhanced Raman spectroscopy, Nat. Commun. 15 (2024) 5624, https://doi.org/10.1038/s41467-024-49973-9.

[59] Z. Cai, H. Weinstein, I. Aravind, R. Li, S. Weng, B. Zhang, J.L. Habif, S.B. Cronin, Dynamic study of intercalation/Deintercalation of ionic liquids in multilayer graphene using an alternating current Raman spectroscopy technique, J. Phys. Chem. Lett. 14 (2023) 7223–7228, https://doi.org/10.1021/acs.jpclett.3c01686.

[60] L. Jaber-Ansari, K.P. Puntambekar, H. Tavassol, H. Yildirim, A. Kinaci, R. Kumar, S. J. Saldaña, A.A. Gewirth, J.P. Greeley, M.K.Y. Chan, M.C. Hersam, Defect evolution in graphene upon electrochemical Lithiation, ACS Appl. Mater. Interfaces 6 (2014) 17626–17636, https://doi.org/10.1021/am503715g.

[61] A. Guéguen, P. Novák, E.J. Berg, XPS study of the Interface evolution of carbonaceous electrodes for Li-O $_2$ batteries during the 1st cycle, J. Electrochem. Soc. 163 (2016) A2545–A2550, https://doi.org/10.1149/2.0351613jes.